npj | 2D materials and applications

Published in partnership with FCT NOVA with the support of E-MRS

Article

https://doi.org/10.1038/s41699-025-00559-z

Carbon-contaminated topological defects in hexagonal boron nitride for quantum photonics

Rohit Babar [1,2] ✉, **Ádám Ganyecz** [1,2], **Igor A. Abrikosov** [3], **Gergely Barcza** [1,2] & **Viktor Ivády** [2,3,4] ✉

Topological defects, such as Stone-Wales defects and grain boundaries, are common in 2D materials. In this study, we investigate the intricate interplay of topological defects and carbon contamination in hexagonal boron nitride revealing an intriguing class of color centers. We demonstrate that both carbon contamination and strain can stabilize Stone-Wales configurations and give rise to emitters with desirable optical properties in the visible spectral range. Inspired by these results, we further demonstrate that carbon atoms at grain boundaries can resolve energetic B-B and N-N bonds leading to highly favorable atomic structures that may facilitate the accumulation of carbon contamination at the boundaries. Similarly to contaminated Stone-Wales defects, carbon-doped grain boundaries can also give rise to color centers emitting in the visible spectral range with short radiative lifetime and high Debye-Waller factors. Our discoveries shed light on an exciting class of single photon emitters in hBN that may be readily observed in grained samples and created by irradiating carbon containing hBN flakes.

Wide-bandgap layered semiconductors have recently emerged as a capable platform for developing integrated photonic devices[1,2]. Similar to conventional bulk semiconductors, atomic-scale structural defects in these materials can implement single photon sources with desirable optical properties[3]. While layered materials may contain defects and impurities in high concentrations, exfoliation of the layered structure provides an ultimate method to control the number of defects in the sample. Thin flakes may contain emitters in such a low number that individual emitters can be resolved by confocal microscopy[4]. Furthermore, due to the absence of internal reflection in thin samples, photons emitted by the color centers can be collected with near unity efficiency[5–7]. These attributes make layered semiconductors a desirable platform for integrated photonics.

Hexagonal boron nitride is famous for its applicable single photon sources[8,9] emitting in a broad spectral range starting at the near-infrared region[10], involving the visible spectrum[11,12], and finishing at the UV-B ultraviolet spectral region[13]. It is generally accepted today that these emitters are related to structural defects of the lattice forming deep levels in the 6.1 eV band gap of hBN. The emitters that have been reported in the literature possess a wide variety of properties, some of them exhibit a bright emission in the zero-phonon line (ZPL)[8], while others emit in a broad spectrum. It has been recently demonstrated that carbon contamination plays a crucial role in the fabrication of visible quantum emitters[14–16].

Despite the numerous experimental and theoretical studies[9], the microscopic structure of most of the emitters is yet to be revealed. A plethora of native[17–19] and impurity-related defects[20–28] has been computationally studied in an attempt to account for the experimental observations. Except for a few examples[17,28], no consensus has been achieved so far regarding the microscopic origin of the emitters. This raises the question of whether all the relevant defect structures have been taken into consideration.

It is known from studies on graphene that the formation of topological defects, such as the Stone-Wales (SW) defects[29] and grain boundaries[30] in the honeycomb lattice of graphene is common. The formation of SW defect in hBN is, however, less favorable, due to the polarized nature of the B-N bonds[31]. Indeed, the formation energy of the 5-7 ring SW defect is as high as 7.2 eV[32–34] in hBN compared to the 5.1 eV of graphene SW defect[35]. These results suggest that topological SW defects are less common in hBN. It is worth mentioning that low-energy irradiation may provide sufficient energy to the lattice to form various SW defects, see Ref. 36.

The formation of grain boundaries, featuring various types of topological defects, is governed not only by thermodynamics but also by the conditions of the growth. In particular, simultaneous nucleation of hBN

---

[1] Wigner Research Centre for Physics, PO Box 49, H-1525, Budapest, Hungary. [2] MTA-ELTE Lendület “Momentum” NewQubit Research Group, Pázmány Péter, Sétány 1/A, 1117 Budapest, Hungary. [3] Department of Physics, Chemistry and Biology, Linköping University, SE-581 83, Linköping, Sweden. [4] Department of Physics of Complex Systems, Eötvös Loránd University, Egyetem tér 1-3, H-1053 Budapest, Hungary. ✉e-mail: rohit.babar@wigner.hun-ren.hu; ivady.viktor@ttk.elte.hu

seeds on the substrate may lead to hBN grains of different orientations, reversed edges, and various relative shifts deviating from the periodicity of the hBN lattice. The interfaces of such grains give rise to various grain boundaries, which form topological line defects[37,38]. Grain boundaries in hBN have been observed by transmission electron (TEM), scanning tunneling (STM) and atomic force microscopy (AFM)[36,39–45] and studied computationally by density functional theory (DFT)[46–48]. Recently, quantum emitters from grain boundaries in hBN have been reported[14,49–53]. Bright emitters along lines in hBN have been speculated to be related to SW defects[49]. Furthermore, cathodoluminescence (CL) study reveals 5.46 and 5.63 eV emission lines (D series) localized at extended defects in hBN[54,55]. Their origin is attributed to excitons bound to grain boundary, dislocations[55,56] or stacking faults[57,58]. Recently, the presence of PL and CL emission around 2.3 eV is proposed to originate from an array of dislocations[59].

In this article, we show that the formation energy of topological defects can be reduced by incorporating carbon contamination into the structure. To demonstrate this, we study a set of carbon-containing Stone-Wales defects (SW-C), with 5-7 rings and 1-4 carbon contaminants in different charge states. In addition, we study 10 different types of grain boundaries and numerous carbon dimer configurations adjacent to them. We show that the formation energy of SW-C defects and carbon dimers at certain positions of the grain boundary is significantly reduced. We also show that applying tensile strain to the hBN sample further favors the formation of SW-C defect. Furthermore, we study the energy balance of different grain boundary-adatom configurations and conclude that mobile carbon atoms may accumulate at the grain boundaries potentially forming stable carbon-contaminated line defects. Finally, we show that SW-C defects and favorable carbon dimers at the grain boundary can give rise to color centers with short excited state lifetime and high Debye-Waller factor in the visible spectral region. The optical properties of the studied defect structures resemble the signatures of the not yet identified carbon-related defects in hBN.

Results and discussions

Formation energy of carbon-containing Stone-Wales defects in hBN

In Fig. 1 we depict the considered Stone-Wales and carbon-containing Stone-Wales configurations. In a pristine hBN layer, the 5–7 SW defect can be obtained by "rotating" a first neighbor B-N pair by 90°, see Fig. 1a. The numbers 5 and 7 indicate the number of vertices of polygons forming the SW defect. In addition to the 5-7 SW defect, we investigate various SW-C structures obtained from carbon substitutional defects by rotating either a C-N, a C-B, or a C-C bond by 90°. In Fig. 1(b), we depict the resulting configurations including either one, two, three, or four carbon atoms. We note that not all the possible configurations are depicted in Fig. 1. We focus on those configurations where the carbon atoms are connected and centered around the shared atoms of the 5 and 7 rings, see Fig. 1. In general, we find these configurations to be energetically more favorable, see related results later and in the Supplementary Information 1. Furthermore, we note that the SW-C_B, SW-C_N, and SW-C_2 configurations tend to buckle the 2D hBN flake at the defect site. Such out-of-plane relaxations are not observed for other SW configurations containing more than two carbon atoms.

Next, we compute the formation energy of the SW-C defects and compare them to the corresponding carbon substitutional defects using the following expression

$$F^{D,q}(E_F,\mu) = E_{\mathrm{tot}}^{D,q} - E_{\mathrm{tot}}^{\mathrm{pure}} - \sum_i n_i\mu_i + qE_F + E_{\mathrm{corr}}(q) \qquad (1)$$

where $F^{D,q}$ is the formation energy of the defect D in charge state q, $E_{\mathrm{tot}}^{D,q}$ and $E_{\mathrm{tot}}^{\mathrm{pure}}$ are the total energies of the defected supercell in charge state q and pristine hBN supercell, respectively, n_i refers to the number of atoms added or removed from the supercell to create defect D, μ_i are the chemical potentials of the atoms added or removed calculated from their energetically preferred structure, E_F is the Fermi energy with reference to the valence band maximum, and $E_{\mathrm{corr}}(q)$ is the correction to the formation energy for charged defects. The charge correction is obtained using supercell scaling method[60]. The thermodynamic equilibrium condition is expressed as $\mu_B + \mu_N = \mu_{BN}$, where μ_{BN} is the total energy per unit cell of hBN. During defect formation, conditions may deviate from equilibrium, leading to an abundance of either nitrogen (N-rich) or boron (N-poor) atoms. Consequently, μ_N in the above expression is set to the gas phase of nitrogen for the N-rich condition, and μ_B for N-poor condition is taken from α-boron. For carbon, μ_C is set to the total energy of graphite per atom.

As shown in Fig. 2 the formation energy of planar SW-C structures is lowered by replacing 1, 2, 3, or 4 boron and nitrogen atoms of the SW defect. Under N-rich (N-poor) condition, the carbon substitution at boron (nitrogen) sites is preferred. We consider the case of N-rich condition to highlight the effect of increasing carbon atoms in SW defect. In the absence of carbon, the SW-hBN prefers the neutral charge state throughout the hBN band gap. Replacing one boron by carbon results in 10% reduction of the formation energy in the upper half of the band gap where the Fermi energy is located. Replacing the boron and nitrogen atoms in between the 5 and 7 atoms rings results in an even larger, 20% reduction of the formation energy of the SW configurations. Including three carbon atoms in the SW configuration reverses the trend compared to the SW-C_2 configuration. Finally, including 4 carbon atoms in the SW structure lowers the energy compared to the SW-C_2 configuration.

To pin the position of the Fermi energy, one must take into account all abundant defects, including vacancy defects and common contaminants in hBN, along with their possible charge states. Our study focuses solely on SW-C family of defects, and thus we cannot assign a Fermi energy in the formation energy plots. An earlier work demonstrated that in the case of carbon defects, the neutral charge state is most favored in the absence of other contaminations, such as oxygen[61]. We anticipate similar trends for SW-C defects and thus investigate the neutral defects later in this article.

To further understand the energetics of SW-C defects and disentangle the effect of carbon contamination on the SW defect from the influence of chemical potential and other factors contributing to the formation energy, we compute the *relative* formation energy of the SW-C defects compared to

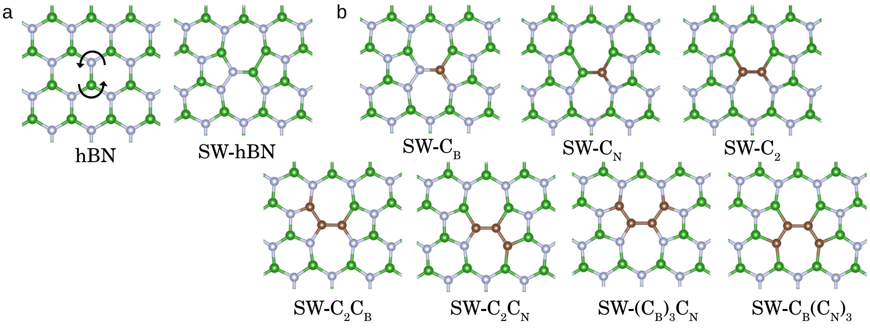

Fig. 1 | Stone-Wales defect in pure and carbon doped hBN. a The ideal honeycomb lattice of hBN transforms to SW defect through a bond rotation indicated by the curved arrows. **b** SW-C defect counterparts for the most prevalent carbon clusters in hBN. Green, gray, and brown spheres denote boron, nitrogen, and carbon atoms respectively. The atomic structures are visualized using VESTA software[100].

Fig. 2 | Formation energies of SW-C defects as a function of the Fermi energy under N-rich and N-poor conditions. The slope of the segments indicates the charge state, while the intersection point of the segments represents the charge transition level. The formation energies of the corresponding substitutional carbon defects in their neutral charge state are indicated by the crosses (×) on the vertical axis.

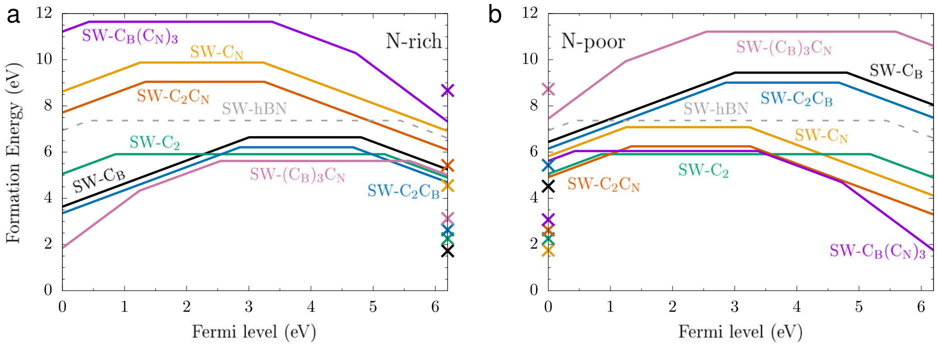

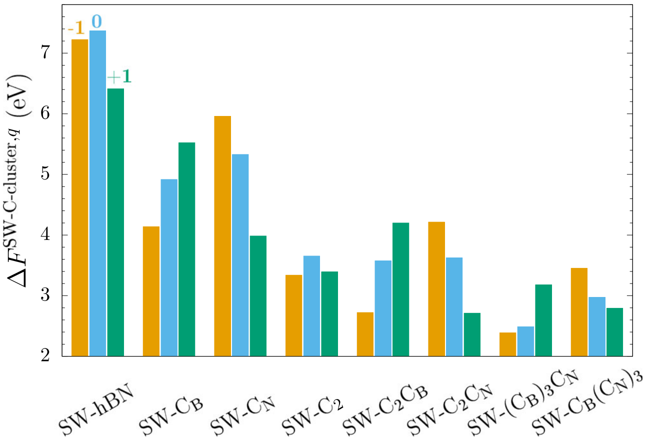

Fig. 3 | Formation energy differences of SW-C defects and corresponding carbon substitutions complexes for different charge states, negative (amber columns), neutral (light blue columns), and positive (green columns). The formation energy differences of the C-related and the corresponding SW-C defect are comparable at those Fermi energy values where they both possess the same charge state. The neutral charge state of SW-C defects is of the highest practical relevance.

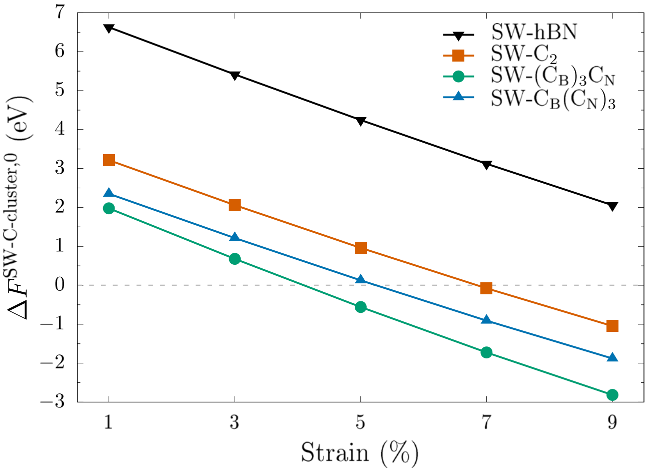

Fig. 4 | Relative formation energies for SW-C defects under tensile strain. The SW-C defects are favorable for 4-7% strain, applied parallel to the SW bond. Here, ΔF refers to the formation energy difference between the substituted carbon cluster and corresponding SW-C configurations. A negative value denotes the favorable formation of SW-C defects.

the formation energy of the corresponding carbon substitutional defect in charge state q as

$$\Delta F^{\mathrm{SW-C-cluster},q} = F^{\mathrm{SW-C-cluster},q} - F^{\mathrm{C-cluster},q} = E_{\mathrm{tot}}^{\mathrm{SW-C-cluster},q} - E_{\mathrm{tot}}^{\mathrm{C-cluster},\,q}, \tag{2}$$

where $E_{\mathrm{tot}}^{\mathrm{SW-C-cluster},\,q}$ and $E_{\mathrm{tot}}^{\mathrm{C-cluster},\,q}$ are the total energies of defective supercells in charge state q. $\Delta F_{\mathrm{rel}}^{\mathrm{SW-C-cluster}}(q)$ measures the energy cost of transforming an existing carbon impurity (cluster) into a related SW-C configurations. Since carbon contamination can be found in hBN in high concentrations, here we discard the energy cost of forming carbon substitutional defects and clusters. The total energy difference can be equal to the difference of the formation energy[62] of the defects assuming the following requirements are fulfilled: (a) the structures contain the same number of atoms, (b) the finite size corrections for the total energy of the SW-C-cluster and the C-cluster are approximately equal and thus they cancel out, and (c) there exists a Fermi energy interval in the band gap of hBN, where both defects possess the same charge state. Condition a) is trivially fulfilled in our simulations, while condition b) should be ensured by the large models considered in our calculations. Condition c) is fulfilled mostly for the neutral charge state, see Fig. 2.

As shown in Fig. 3, the relative formation energy of planar SW-C structures reduces significantly by replacing 1, 2, 3, or 4 boron and nitrogen atoms of the SW defect. In the neutral charge state, replacing one boron (nitrogen) with a carbon atom results in a 33% (27%) reduction of the relative formation energy of the SW configurations. Replacing the boron and nitrogen atoms in between the 5 and 7 atoms rings results in an even larger, 50% reduction of the relative formation energy of the SW configurations. Including three carbon atoms in the SW configuration does not decrease the formation energy further compared to the SW-C$_2$ configuration. Finally, including 4 carbon atoms in the SW structure considerably lowers the energy differences compared to the SW-C$_2$ configuration.

To explain our observations, we start with a discussion of the stability of the SW configuration. In the case of the hBN-SW defect, B-B and N-N bonds are formed, which are energetically unfavorable. Incorporating carbon impurities in the structure relaxes the frustrated bonds through the replacement of B-B and N-N bonds with C-N and C-B bonds. The energy gain for replacing the B and N atoms shared by the 5 and 7 rings is 2.4 eV and 2.0 eV, respectively. The carbon substitution at the next neighbor site that resolves only one-half of the frustrated bond is less favorable in case of SW-C$_B$ while such an arrangement is preferred for SW-C$_N$. When both middle atoms are replaced by carbon, the energy gain is approximately the sum of these two contributions, i.e. 3.7 eV. Two carbon atoms can resolve both energetically unfavorable bonds of the hBN-SW defect. The inclusion of disjoint clusters of carbon atoms at the periphery of the SW defect does not significantly affect the formation energy, thus the configurations depicted in Fig. 1 can be considered the most favorable ones for a given stoichiometry.

Considering the charge state dependence of the relative formation energy of the SW-C defects, we observe a clear pattern for an odd number of

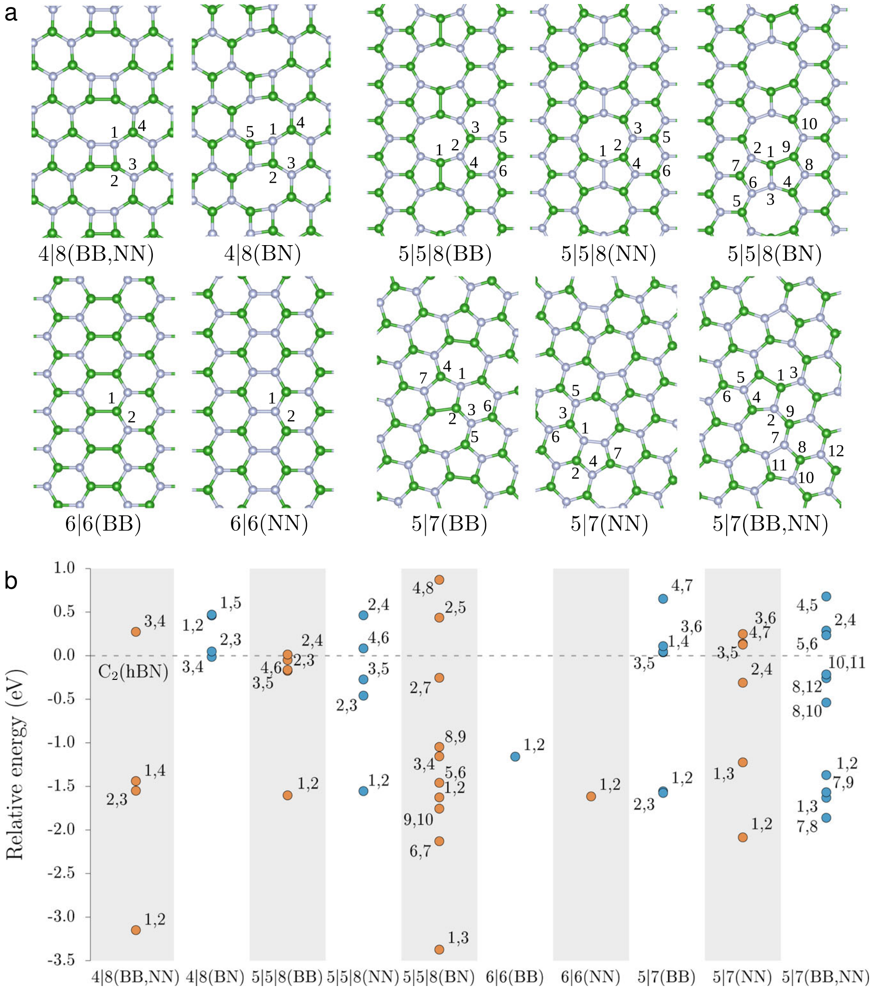

Fig. 5 | Carbon substitution at the grain boundaries. a Grain boundaries and unique sites for carbon substitution considered in our study. **b** Favorable sites for carbon dimer at the grain boundary. Amber and blue dots show the formation energy of carbon dimers at the numbered sites close to the grain boundary. The gray dashed line denotes the reference energy for the carbon dimer away from the respective grain boundary.

carbon atoms. When more boron atoms are substituted by carbon than nitrogen, i.e. SW-C_B, SW-C_2C_B and SW-$(C_B)_3C_N$, the negative charge further stabilizes the SW configuration, while the positive charges increase the energy of the SW configuration, see Fig. 2. The opposite is true for the SW-C defects where more N atoms are replaced by carbon atoms than boron atoms. For an equal number of carbon atoms substitution, no clear relationship between the charge state and the relative formation energy is observed.

The SW configuration introduces highly anisotropic strain in the hBN lattice, which can help to relax external uniaxial stress. Consequently, the formation of SW configurations is favorable under tension[29]. Therefore, we investigate the effect of strain on the formation energy of SW, SW-C_2, SW-$(C_B)_3C_N$, and SW-C_B $(C_N)_3$ configurations. As can be seen in Fig. 4, a strain applied along the axis passing through the shared atoms between the 5 and 7-atom rings further reduces the relative formation energy of the SW-C defects. Due to the lower relative formation energy of the SW-C defects than the hBN SW defect, the SW-C defect may become more favorable than the corresponding non-topological carbon cluster for an applied strain as large as 4–7%. For scale, tensile strain of 6% has been reported in experiments on free-standing monolayer hBN[63], while the theoretical limit is 18% strain[64]. We observe that the lower the relative formation energy of the SW-C defects the lower the strain needed to make the SW-C configuration favorable. Therefore, we anticipate that strained regions in hBN with a high concentration of carbon atoms may host SW-C defects. Furthermore, irradiation of carbon contaminated hBN samples may lead to the formation of carbon containing topological defects.

Formation energy of carbon dimers at grain boundaries

The formation of isolated carbon-containing Stone-Wales defects may still be hindered by the relatively low yet positive formation energy of the structures. However, the growth of hBN has the potential to give rise to grain boundaries, inevitably leading to the formation of Stone-Wales-like defects. In hBN, such grain boundaries comprise of line defects that incorporate different types of B-N rings, most often 4,5,6,7, and 8-atom rings, in a certain sequence. Details of the line defect formed depend on the relative orientation and position of the hBN grains interfacing at the grain boundary. In this section, we investigate the potential of carbon contamination to stabilize high energy bonds at grain boundaries, similar to the case of isolated Stone-Wales defects.

We consider 10 different boundaries as depicted in Fig. 5(a). Most of these grain boundaries have been observed experimentally either in isolated or combined form[36,39,40,42,44] and studied computationally[46,47,65]. To distinguish different grain boundaries, we introduce the following notation: integers i, j, and k separated by vertical lines, such as $i|j|k$, define the number of atoms forming the B-N rings at the grain boundary, while letter pairs in parentheses characterize the bonding (B-B, B-N, and N-N) at the interface. The examined grain boundaries can be categorized into four distinct groups based on the sequence of the different B-N rings, i.e., there are two 4|8, three 5|5|8, two 6|6, and three 5|7 type grain boundaries. To accommodate these line defects in periodic supercells, we use a set of single-layer periodic models and nano-ribbons terminated with hydrogen atoms at the edges, see Methods for details. It is worth mentioning that the formation energy of the different types of grain boundaries can differ significantly, however, their appearance is governed not only by thermodynamics but also by the

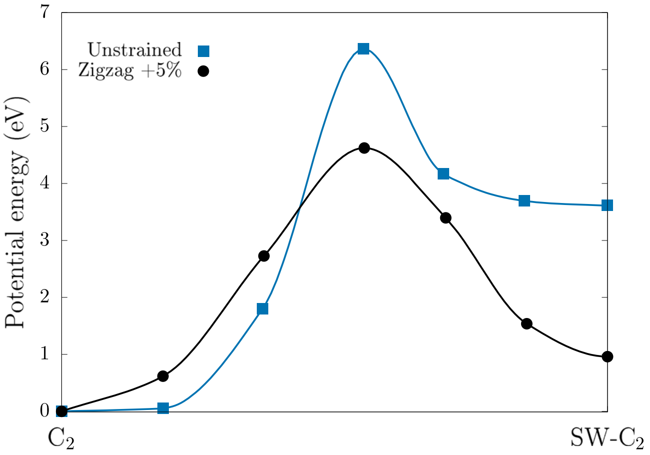

Fig. 6 | Barrier energy for transformation of substituted C_2 defect to SW-C_2. The barrier energies are calculated for the unstrained (blue) and uniaxial tensile strained (black) hBN monolayer.

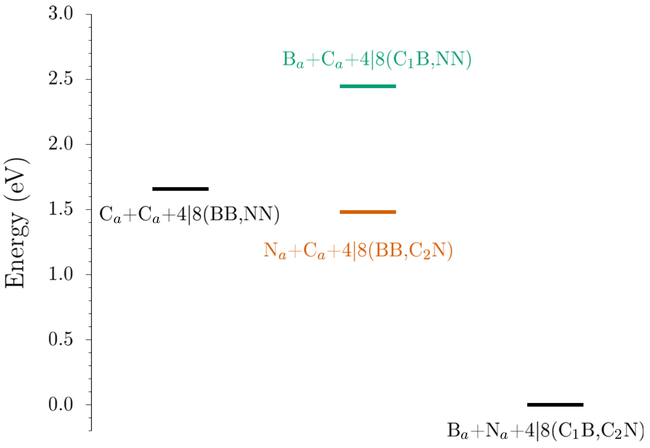

Fig. 7 | Energetics for carbon dimer formation at the 4|8(BB,NN) grain boundary. Colored lines with labels indicate the energy of different configurations of a system of a single-layer grain boundary and two adatoms. The number of atoms and electrons are the same in all configurations, thus the energies are directly comparable. C_a, B_a, and N_a label different adatoms, while 4|8(BB,NN), 4|8 (C_1B,NN), 4|8 (BB,C_2N), and 4|8 (C_1B,C_2N) label grain boundary configurations with no carbon contamination, one carbon atom substituting the boron atom at site 1, one carbon atom substituting the nitrogen atom at site 2, and two carbon atom substituting both the boron atom at site 1 and the nitrogen atom at site 2, respectively. The adatoms are placed far away from the grain boundary in all cases. We note that the energies may be lowered depending on the charge states[101].

nucleation and growth of the BN nano-flakes. Earlier theoretical studies calculate the grain boundary formation energies between 0.2–1.4 eV/Å depending on the bonding and chemical potential[42,46,48,65]. High formation energy boundaries can also be observed in experiments[42].

In the following, we consider one type of carbon defect at the grain boundaries, namely the highly stable carbon dimer[20,61]. Within each grain boundary type, we identify a non-exhaustive set of atomic sites close to the boundary and number them from 1 to 12, see Fig. 5(a). In addition, we consider an adjacent B-N pair far away from the boundary, referred to as far site hereinafter (not shown in Fig. 5(a)). We introduce carbon dimers by replacing adjacent B and N atoms at the numbered sites as well as at the far site. The carbon dimers are referred to as C_x-C_y, where x and y site indexes are specified in Fig. 5(a). B-B and N-N first neighbor pairs are not considered in our study to avoid dependence of the relative formation energy on the chemical potential of boron, carbon, and nitrogen, which may overwhelm the trends we are interested in. This way we directly compare the formation energy of the near-site dimers to the far-site dimer. The far-site carbon dimer is at least 12 Å away from the grain boundary, where the dimer experiences a bulk-like environment. Due to the large number of models and defect configurations considered, we use the computationally affordable PBE[66] exchange-correlation functional in the study of the grain boundaries.

Figure 5(b) depicts the relative formation energy of various carbon dimers at different types of grain boundaries compared to the formation energy of the far-site carbon dimer, which serves as the reference for the energy scale. Negative (positive) values mean favorable (unfavorable) configurations compared to the far-site carbon dimer. Our calculations identify several favorable carbon dimer sites at the grain boundaries. Taking a closer look, we can observe a similar trend as for the isolated 5-7 Stone-Wales defects, i.e. replacement of unfavorable B-B and N-N bonds by C-B, C-N, or C-C bond gives rise to a considerable energy gain. In particular, the C_2-C_3 and C_1-C_4 and the C_1-C_2 carbon dimers at the 4|8 (BB,NN) boundary resolve one and two high energetic bonds in the 4-atom ring and lower the formation energy by ~ 1.5 eV and 3.1 eV, respectively. A pair of carbon substitutional defects in the 8-ring is less favorable. In contrast, there are no high energy B-B and N-N bounds at the 4|8 (BN) boundary, thus the formation energies of boundary-carbon dimers are either comparable to or slightly higher than the far-site carbon dimer. Considering the example of 5|5|8 boundaries, we always find high energetic bonds, thus we can identify favorable carbon pairs. For instance, the replacement of any of the B and N atoms at lattice sites 1, 3, 6, and 9 for the 5|5|8(BN) grain boundary gives rise to a stable substitutional carbon dimer where at least one of the frustrated bonds[31] are relaxed. In addition to the high-energy-bond-relaxation mechanism, we observe an additional effect that influences the formation energy. The 5-ring environment with more N atoms is preferred. Similarly, sites 1 and 2 are preferred in 5|5|8 with B-B or N-N bonds at the boundary. In the case of 6|6 grain boundaries, we identify only one dimer site at the junction, which is energetically favorable compared to the far-site dimer, see Fig. 5. Finally, the complex 5|7 grain boundary also shows numerous favorable carbon dimer sites. The energetically most beneficial configurations are those that resolve either a B-B or N-N bound. The energy difference between the most and least favored site in 5|5|8 and 5|7 grain boundaries are comparable to the trends observed for the SW-C_2 (see Supplementary Fig. 1S1) Note that there are also non-stoichiometric carbon dimer configurations when the carbon atoms substitute either an adjacent pair of B atoms or an adjacent pair of N atoms. Since iso-element pairs are unfavorable in BN, carbon substitutions at these sites could also be highly favorable, however, the formation energy would depend on the chemical potential of the involved elements.

Our results clearly show that there are preferred carbon dimer configurations at grain boundaries, where the most favorable ones are resolving the two high-energy B-B or N-N bonds. The formation energy of the most favorable carbon dimer configurations in our study is lower by ~3 eV than the bulk-like configuration. Taking into consideration the 2.2 eV formation energy (obtained with HSE(0.4) functional) of the carbon dimer in bulk hBN[20], the formation energy of the most favorable carbon dimers at the grain boundary becomes negative. This is only possible by lowering the formation energy of the grain boundary itself. Our results in agreement with Refs. 47,65 show that carbon atoms can further stabilize grain boundaries by replacing high-energy bonds.

Kinetic stability and dynamical processes of SW-C defect formation

In order to assess the stability of the SW-C defects, we study the height of the energy barrier between the substitutional carbon cluster and the corresponding SW-C configuration. In thermal equilibrium, the probability of the stable and the metastable configurations is determined by the formation energy difference of the configurations. At low temperatures, when $k_BT << E_b$, where E_b is the reaction barrier between the two configurations, the atomic configuration may stuck in a higher energy configuration.

Figure 6 depicts the reaction pathway and corresponding energy for transforming a C_2 cluster into a SW-C_2 configuration. We considered both

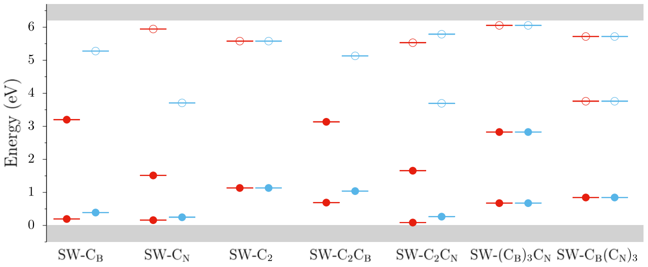

Fig. 8 | Kohn-Sham electronic structure of various neutral SW-C defects in hBN. Red and light blue lines depict spin-up and spin-down Kohn-Sham energy levels between the valence band and the conduction band (gray bars). The occupation of the defect states is indicated by filled and empty spheres. The electronic structure is obtained by using HSE(0.32) exchange-correlation functional.

Table 1 | Ground state spin, ZPL energy, excitation lifetime of the considered SW-C defects in hBN. The ZPLs are obtained on HSE(0.32) level of theory

Defect	Spin	ZPL (eV)	τ (ns)	DW
SW-C$_B$	1/2	1.96	44.8	
SW-C$_N$	1/2	1.17	3.0×10^3	
SW-C$_2$	0	3.93	2.6	0.18
SW-C$_2$C$_B$	1/2	2.12	27.1	
SW-C$_2$C$_N$	1/2	2.74	7.8	
$(\mathrm{SW}-\mathrm{C_B})_3\mathrm{C_N}$	0	2.62	15.1	0.09
SW-C$_B$ (C$_N$)$_3$	0	2.76	8.5	0.15

strained and unstrained hBN sheets. The energy barrier of the $C_2 \rightarrow$ SW-C_2 process is found to be 6.3 eV, while the barrier for the reversed process is 2.7 eV. Considering the intermediate steps of the transition, the highest energy point is associated with the 56° rotated and buckled configuration of the carbon dimer. We estimate the transformation rate for $C_2 \rightarrow$ SW-C_2 from the Arrhenius expression, $\nu = \nu_0\, e^{-E_b/k_B T}$ where ν_0 is the prefactor related to atomic vibrations (typically 10^{14} s^{-1}). At ambient temperature T = 300 K, the transformation rate is 10^{-92} s^{-1} and for annealing temperature of T = 1000 K, the rate lowers to 10^{-18} s^{-1}. We conclude that both the carbon clusters and the SW-C defect are kinetically stable under ambient temperatures, i.e. no transition is expected between the stable and metastable configurations.

These findings are not in favor of the formation of SW and SW-C defects. On the other hand, as demonstrated for graphene, there are alternative mechanisms that can give rise to SW and SW-C defects in hBN. The recombination of divacancy and a mobile carbon adatom can yield a SW-like defect in graphene[67], while a nitrogen-containing vacancy can lower the barrier to form SW-N in graphene[68]. Here, the sliding motion of lattice-carbon atom facilitates the absorption of migrating atoms. In addition, irradiation may transfer sufficient amount of energy to the lattice to form SW and SW-C configurations. Such transition may be more frequent for C clusters than for pristine hBN, due to the lower formation energy and lower energy barrier of the former. Taking into account the positive effect of tensile strain on the formation of SW-C defects, such defects may form in higher concentration at strained areas under irradiation.

According to a recent theoretical work in Ref. 18, carbon and boron interlayer interstitial atoms are mobile at room temperature. Therefore, they either diffuse out from the layers or recombine with another defect in lattice. We study the energetics of various steps of mobile carbon atom-grain boundary recombination. As an example, we consider the case of 4|8 (BB,NN) grain boundary and two carbon adatoms.

Figure 7 shows the local minima of the configuration energy landscape of a 4|8 (BB,NN) grain boundary with two carbon adatoms. Going from left to right, the carbon adatoms replace the boron and nitrogen atoms one by one and on the right reach an energetically favorable configuration where the two carbon atoms are incorporated into the hBN layer and a boron and a nitrogen atom are kicked out. Substituting the boron atom at the grain boundary is energetically unfavourable, however, the substitution of the nitrogen atom and creation of the nitrogen adatom is favoured. Importantly, substituting the adjacent B-N pair at the boundary with carbons, C$_1$-C$_2$ configurations, and creating both boron and nitrogen adatoms is energetically highly beneficial for the system. The substitution of B-N with C-C pair are frequently observed in TEM studies[69]. Similarly, DFT study shows the absorption of carbon pair in 5|7 grain boundaries can aid the migration and bond rotation in defected areas[70]. Therefore, we conclude that the incorporation of carbon atoms at the grain boundaries, even at the cost of displacing nitrogen and boron atoms is preferential, which may lead to the accumulation of carbon atoms and the formation of carbon-contaminated topological defects at the grain boundaries.

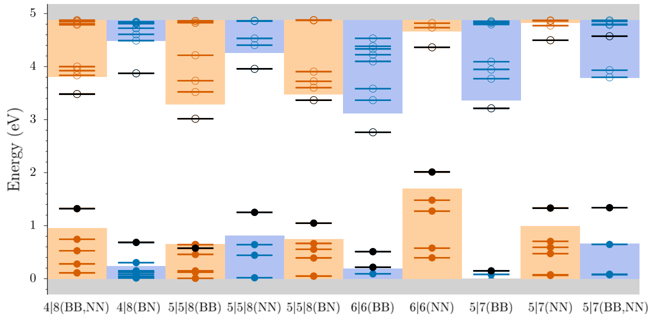

Fig. 9 | PBE Kohn-Sham electronic structure of different highly stable grain boundary carbon dimer configurations in the neutral charge state in hBN. Colored lines with filled and empty circles indicate occupied and unoccupied Kohn-Sham energy levels in the bandgap of hBN. The valance band maximum and the conduction band minimum of pristine hBN are depicted by gray bands. Black lines denote electronic states localized on carbon atoms. The colored (amber and light blue) bars indicate the position of the grain boundary states when no carbon contamination is included in the model. The electronic structures are obtained by using the PBE exchange-correlation functional, which underestimates the energy gaps. Nevertheless, the PBE results are qualitatively valid.

Electronic structure and optical properties

In the previous sections, we analyzed the formation energy, stability, and alternatives of formation of carbon-contaminated SW configurations and grain boundaries. The appearance of the SW-C defects and related configurations may play a role in defining the electrical, optical, and magnetic properties of hBN samples. Considering magnetism, we either find singlet, spin-0, or doublet, spin-1/2, ground state for the SW-C defects and carbon-containing grain boundaries depending on the parity of the total number of electrons, see Fig. 8 and Table 1. For carbon dimers in the SW-C and grain boundary configurations, we obtain a spin-singlet ground state due to the even number of electrons in the neutral charge state, see Figs. 8 and 9. Since none of the studied configurations possess a high-spin ground state, we anticipate that these defects cannot implement spin qubits in hBN. On the other hand, we find both occupied and unoccupied defect states in the bandgap of hBN for the SW-C defects, see Fig. 8, as well as for the energetically favorable carbon-contaminated grain boundary configurations, see Fig. 9.

In the neutral charge state, most of the configurations exhibit occupied defect states in the lower half of the bandgap and unoccupied states in the upper half of the bandgap. Similar trends are observed in C-SW defects in hBN and nanotubes[34,71,72]. We anticipate from these observations that the neutral charge state of most of the SW-C and carbon dimer containing grain boundary defect configurations is stable when the Fermi energy is in the middle of the band gap of hBN.

It is worth noting that the band gap of grain boundary models is significantly reduced compared to pristine hBN, due to the quasi-localized

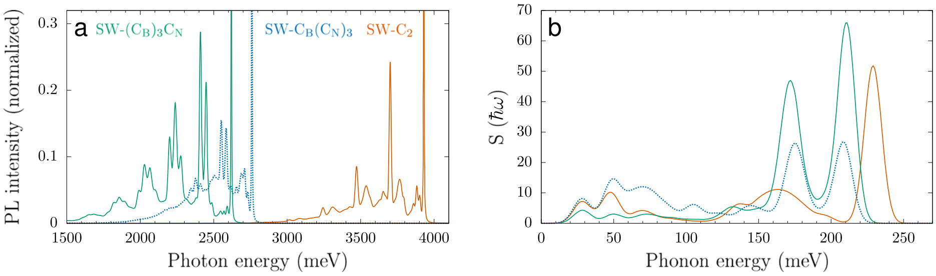

Fig. 10 | Calculated photoluminescence spectra and phonon energy spectral function for select SW-C defects. **a** The left panel denotes the normalized PL spectra for SW-C_2 (orange), SW-$(C_B)_3C_N$ (green) and SW-C_B $(C_N)_3$ (blue) defects. **b** While the right panel shows the spectral function S for phonon modes contributing to the PL spectra. The unequal carbon bonds of SW-$(C_B)_3C_N$ result in two phonon sidebands at 171 and 210 meV.

Table 2 | ZPL energy, excitation lifetime of the highly stable carbon dimers at 4|8 grain boundaries in hBN. The ZPLs are obtained on HSE(0.32) level of theory

Grain boundary	Configuration	ZPL (eV)	τ (ns)	DW
4|8 (BB,NN)	C_1-C_2	2.72	16.6	0.02
4|8 (BN)	C_3-C_4	3.84	2.0	0.24

grain boundary states. The 4.8 eV PBE band gap of hBN reduces to 2.6–4.2 eV, in particular 4|8(BB,NN): 2.8 eV, 4|8(BN): 4.2 eV; 5|5|8(BB): 2.6 eV; 5|5|8(NN): 3.4 eV; 5|5|8(BN): 2.7 eV; 6|6(BB): 2.9 eV; 6|6(NN): 2.9 eV; 5|7(BB): 3.8 eV; 5|7(NN): 3.9 eV; 5|7(BB,NN): 3.1 eV, see colored shaded areas in Fig. 9. Since both the conduction and the valence band edges are affected by the grain boundary states, grain boundaries can act as charge carrier traps. Furthermore, we notice in the calculations that the energy of the grain boundary states is often altered by the carbon dimer, which indicates strong hybridization between the states of the line and point defects.

In Figs. 8 and 9, all the electronic structures exhibit at least one occupied as well as at least one unoccupied defect state in the band gap of either hBN or the considered grain boundary configuration. These results suggest that the SW-C configurations and carbon dimers at the grain boundary can give rise to color centers in the visible spectral range. In low defect concentrations, they may behave like single photon emitters in hBN.

To further investigate this possibility, we first calculate the zero-phonon line (ZPL) energy of different SW-C configurations in hBN using HSE(0.32) functional, which are summarized in Table 1. Similar results are obtained from TD-DFT calculations (see Methods and Supplementary Information 1 for additional details). We find that the SW-C_2 defect emits at around 3.9 eV, while the most favorable four carbon-containing configurations are around 2.7 eV. The estimated error margin of the ZPL values is expected about 0.1–0.2 eV in our calculations. Thus, SW-C_2 and SW-C_4 defects emerge as alternative candidates for the UV and blue emitters[20,73].

In order to estimate the brightness of the SW-C color centers, we calculate the radiative lifetime of the SW-C_2, SW-$(C_B)_3C_N$, and SW-$C_{(B)}$ $(C_N)_3$ configurations. We respectively obtain 2.6 ns, 15.1 ns, and 8.5 ns for the optical lifetime of these defects. Due to the relatively large ZPL and the presumably absent alternative spin shelving states, we expect high quantum efficiency and bright visible emission for these defects. On the other hand, the large radiative lifetime for SW-C_N defect is a combined effect of small transition dipole moment and ZPL energy compared to other defects.

Accordingly, we determine their PL spectra, depicted in Fig. 10. As can be seen, the C-C phonon modes are similar in nature to the carbon substitutional defects albeit with energy shifts corresponding to the altered bond strengths in SW configuration. The Debye-Waller factors for SW-C_2 and SW-$C_{(B)}$ $(C_N)_3$ are found to be comparable to the values predicted for hBN SW and carbon substitutional defects[19,20,74].

We also explore the optical properties of grain boundaries which largely depend on the local bonding at the boundary. Owing to computational demand, we consider only a few highly favorable carbon dimer-containing grain boundary configurations as illustration, see Table 2. We find that the studied configurations emit in a similar spectral range as the SW-C defects. The corresponding radiative lifetime for the most stable carbon dimers in 4|8(BB,NN) and 4|8(BN) is 16.6 ns and 2.0 ns respectively. As shown in Fig. 11 and in Table 2, the C_1-C_2 carbon dimer in 4|8(BB,NN) grain boundary emits in the visible range with a predominant phonon contribution to the PL spectra. In contrast, the UV active C_3-C_4 defect hosted in the 4|8(BN) grain boundary exhibits a significant Debye-Waller factor (0.24). Therefore, we expect other grain boundaries to host bright color centers as well. Point defects may act as a recombination center for excitons and separated electron and hole pairs captured by the quasi-localized states of the grain boundary. Realizing charge carrier injection in such structures may lead to electroluminescence[75,76].

From the computed optical properties of the SW-C defects and carbon-contaminated grain boundaries, we conclude that some of these defects are particularly interesting for quantum photonic applications due to their short lifetime and dominating ZPL emission. In addition, the optical properties of the SW-C defect resemble the carbon-related visible emitters[14,77].

Discussion

In this article, we demonstrated that carbon contamination can play an important role in stabilizing topological defects, such as Stone-Wales defects and grain boundaries in hBN. Carbon Stone-Wales may appear in increased concentration in strained areas of irradiated hBN, while carbon impurities may accumulate at grain boundaries and form a series of highly stable carbon-containing defect structures. We also showed that the studied defects can give rise to bright color centers in hBN emitting in the visible spectral range with desirable optical properties. Based on the similarity of the optical properties, the SW-C defect may serve as a working model for the not-yet-identified carbon-related visible emitters in hBN. While these defects may be readily observed in as-grown samples, imparting sufficient energy to facilitate bond rotation via irradiation may increase the number of SW-C defects. Indeed, recent experiments[78] used such an aftergrowth treatment and reported on an increase of visible emitters.

To verify our models, the alignment of the emission dipole and the crystal lattices may be compared. Due to the 90° rotation of a carbon-related bond in the SW-C defects, the emission dipole. Consequently, correlating crystallographical directions with the emission dipole, one may observe 30°, 90°, and 150° emission dipole orientations compared to one of the inplane axes for simple SW-C configurations. In a very recent measurement, see Fig. 2e in Ref. 78, a similar pattern has been reported. However, more measurements are needed to make conclusions here.

The defects studied in this article not only broaden our understanding of hBN's defect landscape but also point to a potential avenue for identifying previously unknown hBN color centers. Ultimately, our findings may pave the way toward the controlled fabrication of visible emitters in hBN, opening new possibilities for applications in quantum technologies and optoelectronics.

Methods

Density functional theory (DFT) calculations for single-layer hBN models are performed using the Vienna Ab-initio Simulation Package (VASP)[79],

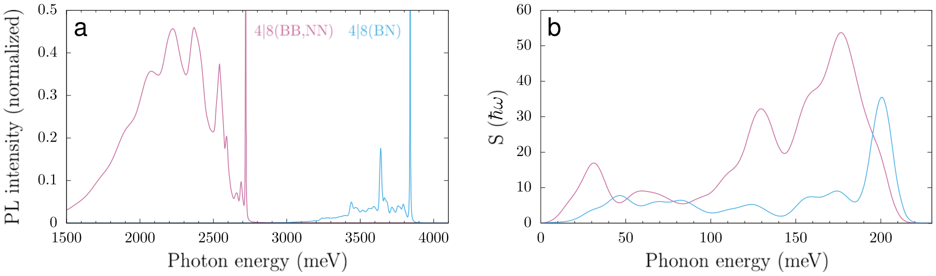

Fig. 11 | Optical properties of carbon dimers at grain boundaries. **a** Calculated photoluminescence spectra and **b** phonon energy spectral function for carbon dimers at grain boundaries 4|8(BB,NN) (pink) and 4|8(BN) (blue).

which utilizes the projector-augmented wave method[80] and a plane-wave basis set. The plane-wave and kinetic energy cutoff are set to 450 and 900 eV, respectively. Exchange-correlation effects of the many-electron system are described by the generalized gradient approximation of Perdew, Burke, and Ernzerhof (PBE)[66] and also the screened hybrid functional of Heyd-Scuseria-Ernzerhof (HSE06)[81] with a modified exact exchange fraction of 0.32 and screening parameter of 0.2 Å $^{-1}$. The HSE06 functional is used to obtain formation energies, ZPL energies and the electronic structure of point defects, while the PBE functional is used in the study of grain boundaries with the exception of ZPL energies that are calculated using HSE06 functional. The van der Waals interaction is included using the Grimme-D3 method[82].

In our study, we consider a 128-atom hexagonal supercell for the SW-C defect calculations including a vacuum of 18 Å between the periodic hBN layers. The grain boundaries are modeled in orthorhombic supercells of dimensions 18–20 Å along with the grain boundary and varying lengths of 30–80 Å in the perpendicular direction. Following the coincidence site lattice theory[83], the periodicity of supercell is retained by including a single, parallel, or antiparallel grain boundary. The electronic structure of carbon dimer containing grain boundaries is also verified in hydrogen-terminated ribbon models for selected cases. The reciprocal space is sampled with Γ-point. Atomic positions are relaxed until the forces are less than 0.01 eV/Å. The bond rotation barrier energies are calculated with PBE functional using the climbing image nudged elastic band method[84,85].

The excited state properties are obtained using a combination of electronic and vibrational calculation setups. The ZPL energy is calculated as the energy difference between ground and excited states, where the excited state configuration is found using Δ-SCF method[86]. In case of defects with singlet spin configuration, we estimate the energy of excited singlet state as $2E(M)$-$E(T)$ where $E(M)$ refers to the energy of default mixed-spin excited state and $E(T)$ is the energy of the relaxed triplet state[20]. The photoluminescence spectra and the Debye-Waller factor are calculated with the PyPhotonics package[87]. Here, the phonon modes are calculated from Phonopy code[88,89] using the finite-displacement method. The grain boundary supercell dimensions are reduced to manage the high computational cost of phonon calculations.

The radiative lifetime is calculated as[90]

$$\tau = \frac{3\pi\epsilon_0 c^3 \hbar^4}{n E_{\mathrm{ZPL}}^3 \mu^2}, \tag{3}$$

where ϵ_0 is the vacuum permittivity, c is the speed of light, n is the refractive index of hBN and μ is the transition dipole moment of the electronic states corresponding to the ZPL. The refractive indices are taken from an ellipsometry study on thin film hBN[91].

To verify the ZPL energies calculated with Δ-SCF method, we carry out time-dependent DFT (TD-DFT) calculation for hBN flake. The vertical and ZPL energy calculations for defects with singlet spin configuration are performed using the ORCA package[92]. A combination of PBE0[93], HSE06, CAM-B3LYP[94] functionals and def2-SVP[95], def2-TZVP, aug-cc-pVDZ[96] basis sets for 58 to 158-atom flakes are considered. The first excited singlet state is identified by invoking five roots in TD-DFT calculation, followed by geometry optimization.

Data availability

The main data supporting the findings of this study are available within the paper and its Supplementary Information 1 (including Refs. 97–99). Further numerical data are available from the authors upon reasonable request.

Received: 10 July 2024; Accepted: 7 April 2025;

References

1. Liu, Y., Fang, Y., Yang, D., Pi, X. & Wang, P. Recent progress of heterostructures based on two dimensional materials and wide bandgap semiconductors. *J. Phys.: Condens. Matter* **34**, 183001 (2022).
2. Li, Z., Yan, T. & Fang, X. Low-dimensional wide-bandgap semiconductors for uv photodetectors. *Nat. Rev. Mater.* **8**, 587–603 (2023).
3. Michaelis de Vasconcellos, S. et al. Single-photon emitters in layered van der waals materials. *Phys. Status Solidi (b)* **259**, 2100566 (2022).
4. Tran, T. T., Bray, K., Ford, M. J., Toth, M. & Aharonovich, I. Quantum emission from hexagonal boron nitride monolayers. *Nat. Nanotechnol.* **11**, 37–41 (2015).
5. Schell, A. W., Svedendahl, M. & Quidant, R. Quantum emitters in hexagonal boron nitride have spectrally tunable quantum efficiency. *Adv. Mater.* **30**, 1704237 (2018).
6. Nikolay, N. et al. Direct measurement of quantum efficiency of single-photon emitters in hexagonal boron nitride. *Optica* **6**, 1084 (2019).
7. Boll, M. K., Radko, I. P., Huck, A. & Andersen, U. L. Photophysics of quantum emitters in hexagonal boron-nitride nano-flakes. *Opt. Express* **28**, 7475 (2020).
8. Caldwell, J. D. et al. Photonics with hexagonal boron nitride. *Nat. Rev. Mater.* **4**, 552–567 (2019).
9. Sajid, A., Ford, M. J. & Reimers, J. R. Single-photon emitters in hexagonal boron nitride: a review of progress. *Rep. Prog. Phys.* **83**, 044501 (2020).
10. Camphausen, R. et al. Observation of near-infrared sub-Poissonian photon emission in hexagonal boron nitride at room temperature. *APL Photonics* **5**, 076103 (2020).
11. Tran, T. T. et al. Robust Multicolor Single Photon Emission from Point Defects in Hexagonal Boron Nitride. *ACS Nano* **10**, 7331–7338 (2016).
12. Chejanovsky, N. et al. Single-spin resonance in a van der Waals embedded paramagnetic defect. *Nat. Mater.* **20**, 1079–1084 (2021).
13. Bourrellier, R. et al. Bright UV Single Photon Emission at Point Defects in h-BN. *Nano Lett.* **16**, 4317–4321 (2016).
14. Mendelson, N. et al. Engineering and tuning of quantum emitters in few-layer hexagonal boron nitride. *ACS Nano* **13**, 3132–3140 (2019).

15. Kumar, A. et al. Localized creation of yellow single photon emitting carbon complexes in hexagonal boron nitride. *APL Mater.* **11**, 071108 (2023).
16. Zhong, D. et al. Carbon-Related Quantum Emitter in Hexagonal Boron Nitride with Homogeneous Energy and 3-Fold Polarization. *Nano Lett.* **24**, 1106–1113 (2024).
17. Ivády, V. et al. Ab initio theory of the negatively charged boron vacancy qubit in hexagonal boron nitride. *npj Comput. Mater.* **6**, 1–6 (2020).
18. Weston, L., Wickramaratne, D., Mackoit, M., Alkauskas, A. & Van de Walle, C. G. Native point defects and impurities in hexagonal boron nitride. *Phys. Rev. B* **97**, 214104 (2018).
19. Hamdi, H., Thiering, G., Bodrog, Z., Ivády, V. & Gali, A. Stone-wales defects in hexagonal boron nitride as ultraviolet emitters. *npj Comput. Mater.* **6**, 1–7 (2020).
20. Mackoit-Sinkevičienė, M., Maciaszek, M., Van de Walle, C. G. & Alkauskas, A. Carbon dimer defect as a source of the 4.1 eV luminescence in hexagonal boron nitride. *Appl. Phys. Lett.* **115**, 212101 (2019).
21. Golami, O. et al. Ab initio and group theoretical study of properties of a carbon trimer defect in hexagonal boron nitride. *Phys. Rev. B* **105**, 184101 (2022).
22. Tawfik, S. A. et al. First-principles investigation of quantum emission from hBN defects. *Nanoscale* **9**, 13575–13582 (2017).
23. Sajid, A., Reimers, J. R. & Ford, M. J. Defect states in hexagonal boron nitride: Assignments of observed properties and prediction of properties relevant to quantum computation. *Phys. Rev. B* **97**, 064101 (2018).
24. Auburger, P. & Gali, A. Towards ab initio identification of paramagnetic substitutional carbon defects in hexagonal boron nitride acting as quantum bits. *Phys. Rev. B* **104**, 075410 (2021).
25. Jara, C. et al. First-principles identification of single photon emitters based on carbon clusters in hexagonal boron nitride. *J. Phys. Chem. A* **125**, 1325–1335 (2021).
26. Cholsuk, C., Suwanna, S. & Vogl, T. Tailoring the emission wavelength of color centers in hexagonal boron nitride for quantum applications. *Nanomaterials* **12**, 2427 (2022).
27. Bhang, J., Ma, H., Yim, D., Galli, G. & Seo, H. First-principles predictions of out-of-plane group IV and V dimers as high-symmetry, high-spin defects in hexagonal boron nitride. *ACS Appl. Mater. Interfaces* **13**, 45768–45777 (2021).
28. Li, S. & Gali, A. Identification of an oxygen defect in hexagonal boron nitride. *J. Phys. Chem. Lett.* **13**, 9544–9551 (2022).
29. Tiwari, S. K. et al. Stone-wales defect in graphene. *Small* **19**, 2303340 (2023).
30. Yazyev, O. V. & Chen, Y. P. Polycrystalline graphene and other two-dimensional materials. *Nat. Nanotechnol.* **9**, 755–767 (2014).
31. Charlier, J.-C., Blase, X., De Vita, A. & Car, R. Microscopic growth mechanisms for carbon and boron-nitride nanotubes. *Appl. Phys. A: Mater. Sci. Process.* **68**, 267–273 (1999).
32. Li, Y. et al. Stone-wales defects in single-walled boron nitride nanotubes: Formation energies, electronic structures, and reactivity. *J. Phys. Chem. C.* **112**, 1365–1370 (2008).
33. Chen, W., Li, Y., Yu, G., Zhou, Z. & Chen, Z. Electronic structure and reactivity of boron nitride nanoribbons with stone-wales defects. *J. Chem. Theory Comput.* **5**, 3088–3095 (2009).
34. Wang, R., Yang, J., Wu, X. & Wang, S. Local charge states in hexagonal boron nitride with stone-wales defects. *Nanoscale* **8**, 8210–8219 (2016).
35. Lusk, M. T. & Carr, L. D. Nanoengineering defect structures on graphene. *Phys. Rev. Lett.* **100**, 175503 (2008).
36. Gibb, A. L. et al. Atomic resolution imaging of grain boundary defects in monolayer chemical vapor deposition-grown hexagonal boron nitride. *J. Am. Chem. Soc.* **135**, 6758–6761 (2013).
37. Auwärter, W., Muntwiler, M., Osterwalder, J. & Greber, T. Defect lines and two-domain structure of hexagonal boron nitride films on Ni(111). *Surf. Sci.* **545**, 735–740 (2003).
38. Dong, G., Fourré, E. B., Tabak, F. C. & Frenken, J. W. M. How boron nitride forms a regular nanomesh on Rh(111). *Phys. Rev. Lett.* **104**, 096102 (2010).
39. Cretu, O., Lin, Y.-C. & Suenaga, K. Evidence for active atomic defects in monolayer hexagonal boron nitride: A new mechanism of plasticity in two-dimensional materials. *Nano Lett.* **14**, 1064–1068 (2014).
40. Li, Q. et al. Grain boundary structures and electronic properties of hexagonal boron nitride on Cu(111). *Nano Lett.* **15**, 5804–5810 (2015).
41. Bayer, B. C. et al. Introducing overlapping grain boundaries in chemical vapor deposited hexagonal boron nitride monolayer films. *ACS Nano* **11**, 4521–4527 (2017).
42. Ren, X., Wang, X. & Jin, C. Atomic-precision fabrication of quasi-full-space grain boundaries in two-dimensional hexagonal boron nitride. *Nano Lett.* **19**, 8581–8589 (2019).
43. Ren, X. et al. Grain boundaries in chemical-vapor-deposited atomically thin hexagonal boron nitride. *Phys. Rev. Mater.* **3**, 014004 (2019).
44. Park, H. J. et al. One-dimensional hexagonal boron nitride conducting channel. *Sci. Adv.* **6**, eaay4958 (2020).
45. Wrigley, J. et al. Epitaxy of boron nitride monolayers for graphene-based lateral heterostructures. *2D Mater.* **8**, 034001 (2021).
46. Liu, Y., Zou, X. & Yakobson, B. I. Dislocations and grain boundaries in two-dimensional boron nitride. *ACS Nano* **6**, 7053–7058 (2012).
47. Li, X., Wu, X., Zeng, X. C. & Yang, J. Band-gap engineering via tailored line defects in boron-nitride nanoribbons, sheets, and nanotubes. *ACS Nano* **6**, 4104–4112 (2012).
48. Ding, N., Wu, C.-M. L. & Li, H. The effect of grain boundaries on the mechanical properties and failure behavior of hexagonal boron nitride sheets. *Phys. Chem. Chem. Phys.* **16**, 23716–23722 (2014).
49. Chejanovsky, N. et al. Structural attributes and photodynamics of visible spectrum quantum emitters in hexagonal boron nitride. *Nano Lett.* **16**, 7037–7045 (2016).
50. Ngoc My Duong, H. et al. Effects of high-energy electron irradiation on quantum emitters in hexagonal boron nitride. *ACS Appl. Mater. Interfaces* **10**, 24886–24891 (2018).
51. Xu, Z.-Q. et al. Single photon emission from plasma treated 2d hexagonal boron nitride. *Nanoscale* **10**, 7957–7965 (2018).
52. Vogl, T., Doherty, M. W., Buchler, B. C., Lu, Y. & Lam, P. K. Atomic localization of quantum emitters in multilayer hexagonal boron nitride. *Nanoscale* **11**, 14362–14371 (2019).
53. Shevitski, B. et al. Blue-light-emitting color centers in high-quality hexagonal boron nitride. *Phys. Rev. B* **100**, 155419 (2019).
54. Watanabe, K. & Taniguchi, T. Jahn-teller effect on exciton states in hexagonal boron nitride single crystal. *Phys. Rev. B* **79**, 193104 (2009).
55. Jaffrennou, P. et al. Origin of the excitonic recombinations in hexagonal boron nitride by spatially resolved cathodoluminescence spectroscopy. *J. Appl. Phys.* **102**, https://doi.org/10.1063/1.2821413 (2007).
56. Pierret, A. et al. Excitonic recombinations in hBN: From bulk to exfoliated layers. *Phys. Rev. B* **89**, 035414 (2014).
57. Watanabe, K., Taniguchi, T., Kuroda, T. & Kanda, H. Effects of deformation on band-edge luminescence of hexagonal boron nitride single crystals. *Appl. Phys. Lett.* **89**, https://doi.org/10.1063/1.2358314 (2006).
58. Bourrellier, R. et al. Nanometric resolved luminescence in h-bn flakes: Excitons and stacking order. *ACS Photonics* **1**, 857–862 (2014).

59. Ciampalini, G. et al. Light emission properties of mechanical exfoliation induced extended defects in hexagonal boron nitride flakes. *2D Mater.* **9**, 035018 (2022).
60. Wang, D. et al. Determination of formation and ionization energies of charged defects in two-dimensional materials. *Phys. Rev. Lett.* **114**, 196801 (2015).
61. Maciaszek, M., Razinkovas, L. & Alkauskas, A. Thermodynamics of carbon point defects in hexagonal boron nitride. *Phys. Rev. Mater.* **6**, 014005 (2022).
62. Gali, A. Ab initio theory of the nitrogen-vacancy center in diamond. *Nanophotonics* **8**, 1907–1943 (2019).
63. Han, Y. et al. Large Elastic Deformation and Defect Tolerance of Hexagonal Boron Nitride Monolayers. *Cell Rep. Phys. Sci.* **1**, 100172 (2020).
64. Peng, Q., Ji, W. & De, S. Mechanical properties of the hexagonal boron nitride monolayer: Ab initio study. *Comput. Mater. Sci.* **56**, 11–17 (2012).
65. Gomes, L. C., Alexandre, S. S., Chacham, H. & Nunes, R. W. Stability of edges and extended defects on boron nitride and graphene monolayers: The role of chemical environment. *J. Phys. Chem. C.* **117**, 11770–11779 (2013).
66. Perdew, J. P., Burke, K. & Ernzerhof, M. Generalized gradient approximation made simple. *Phys. Rev. Lett.* **77**, 3865–3868 (1996).
67. Wu, L., Hou, T., Li, Y., Chan, K. S. & Lee, S.-T. First-principles study on migration and coalescence of point defects in monolayer graphene. *J. Phys. Chem. C.* **117**, 17066–17072 (2013).
68. Hou, Z. & Terakura, K. Effect of nitrogen doping on the migration of the carbon adatom and monovacancy in graphene. *J. Phys. Chem. C.* **119**, 4922–4933 (2015).
69. Krivanek, O. L. et al. Atom-by-atom structural and chemical analysis by annular dark-field electron microscopy. *Nature* **464**, 571–574 (2010).
70. Wang, J., Li, S. N. & Liu, J. B. Migrations of pentagon-heptagon defects in hexagonal boron nitride monolayer: The first-principles study. *J. Phys. Chem. A* **119**, 3621–3627 (2015).
71. Kim, G., Park, J. & Hong, S. First-principles study of substitutional carbon pair and stone-wales defect complexes in boron nitride nanotubes. *Chem. Phys. Lett.* **522**, 79–82 (2012).
72. Anafcheh, M. & Ghafouri, R. Carbon doping of defect sites in stone-wales defective boron-nitride nanotubes: A density functional theory study. *J. Clust. Sci.* **24**, 865–879 (2013).
73. Maciaszek, M. & Razinkovas, L. Blue quantum emitter in hexagonal boron nitride and a carbon chain tetramer: a first-principles study. *ACS Appl. Nano Mater.* **7**, 18979–18985 (2024).
74. Benedek, Z. et al. Symmetric carbon tetramers forming spin qubits in hexagonal boron nitride. *npj Comput. Mater.* **9**, 187 (2023).
75. Rong, Y. et al. Electroluminescence dynamics across grain boundary regions of monolayer tungsten disulfide. *ACS Nano* **10**, 1093–1100 (2015).
76. Kim, G. et al. Blue emission at atomically sharp 1d heterojunctions between graphene and h-bn. *Nat. Commun.* **11**, 5359 (2020).
77. Zhigulin, I. et al. Photophysics of blue quantum emitters in hexagonal boron nitride. *Mater. Quantum Technol.* **3**, 015002 (2023).
78. Kumar, A. et al. Polarization Dynamics of Solid-State Quantum Emitters. *ACS Nano* **18**, 5270–5281 (2024).
79. Kresse, G. & Furthmüller, J. Efficient iterative schemes for ab initio total-energy calculations using a plane-wave basis set. *Phys. Rev. B* **54**, 11169–11186 (1996).
80. Blöchl, P. E. Projector augmented-wave method. *Phys. Rev. B* **50**, 17953–17979 (1994).
81. Heyd, J., Scuseria, G. E. & Ernzerhof, M. Erratum: "Hybrid functionals based on a screened coulomb potential" [j. chem. phys. 118, 8207 (2003)]. *J. Chem. Phys.* **124**, 219906 (2006).
82. Grimme, S., Antony, J., Ehrlich, S. & Krieg, H. A consistent and accurate ab initio parametrization of density functional dispersion correction (DFT-D) for the 94 elements H-Pu. *J. Chem. Phys.* **132**, 154104 (2010).
83. Carlsson, J. M., Ghiringhelli, L. M. & Fasolino, A. Theory and hierarchical calculations of the structure and energetics of [0001] tilt grain boundaries in graphene. *Phys. Rev. B* **84**, 165423 (2011).
84. Henkelman, G. & Jónsson, H. Improved tangent estimate in the nudged elastic band method for finding minimum energy paths and saddle points. *J. Chem. Phys.* **113**, 9978–9985 (2000).
85. Henkelman, G., Uberuaga, B. P. & Jónsson, H. A climbing image nudged elastic band method for finding saddle points and minimum energy paths. *J. Chem. Phys.* **113**, 9901–9904 (2000).
86. Jones, R. O. & Gunnarsson, O. The density functional formalism, its applications and prospects. *Rev. Mod. Phys.* **61**, 689–746 (1989).
87. Tawfik, S. A. & Russo, S. P. Pyphotonics: A python package for the evaluation of luminescence properties of defects. *Comput. Phys. Commun.* **273**, 108222 (2022).
88. Togo, A. & Tanaka, I. First principles phonon calculations in materials science. *Scr. Materialia* **108**, 1–5 (2015).
89. Togo, A. First-principles phonon calculations with phonopy and phono3py. *J. Phys. Soc. Jpn.* **92**, 012001 (2023).
90. Stoneham, A. M.*Theory of defects in solids: electronic structure of defects in insulators and semiconductors* (Oxford University Press, 2001).
91. Schubert, M. et al. Anisotropy of boron nitride thin-film reflectivity spectra by generalized ellipsometry. *Appl. Phys. Lett.* **70**, 1819–1821 (1997).
92. Neese, F. Software update: The orca program system-version 5.0. *Wiley Interdiscip. Rev.: Comput. Mol. Sci.* **12**, e1606 (2022).
93. Adamo, C. & Barone, V. Toward reliable density functional methods without adjustable parameters: The pbe0 model. *J. Chem. Phys.* **110**, 6158–6170 (1999).
94. Yanai, T., Tew, D. P. & Handy, N. C. A new hybrid exchange-correlation functional using the coulomb-attenuating method (cam-b3lyp). *Chem. Phys. Lett.* **393**, 51–57 (2004).
95. Weigend, F. & Ahlrichs, R. Balanced basis sets of split valence, triple zeta valence and quadruple zeta valence quality for h to rn: Design and assessment of accuracy. *Phys. Chem. Chem. Phys.* **7**, 3297–3305 (2005).
96. Dunning, T. H. Gaussian basis sets for use in correlated molecular calculations. i. the atoms boron through neon and hydrogen. *J. Chem. Phys.* **90**, 1007–1023 (1989).
97. Korona, T., Jankowska, J. & Masoumifeshani, E. Dicarbon defect in hexagonal boron nitride 743 monolayer-a theoretical study. *Can. J. Chem.* **101**, 684–697 (2023).
98. Winter, M., Bousquet, M. H. E., Jacquemin, D., Duchemin, I. & Blase, X. Photoluminescent properties of the carbon-dimer defect in hexagonal boron-nitride: A many-body finite-size cluster approach. *Phys. Rev. Mater.* **5**, 095201 (2021).
99. Reimers, J. R., Sajid, A., Kobayashi, R. & Ford, M. J. Understanding and calibrating density-functional-theory calculations describing the energy and spectroscopy of defect sites in hexagonal boron nitride. *J. Chem. Theory Comput.* **14**, 1602–1613 (2018).
100. Momma, K. & Izumi, F. Vesta 3 for three-dimensional visualization of crystal, volumetric and morphology data. *J. Appl. Crystallogr.* **44**, 1272–1276 (2011).
101. Berseneva, N., Gulans, A., Krasheninnikov, A. V. & Nieminen, R. M. Electronic structure of boron nitride sheets doped with carbon from first-principles calculations. *Phys. Rev. B* **87**, 035404 (2013).

Acknowledgements

This research was supported by the National Research, Development, and Innovation Office of Hungary within the Quantum Information National Laboratory of Hungary (Grant No. 2022-2.1.1-NL-2022-00004) and within grants FK 135496 and FK 145395. V.I. and I.A.A. also acknowledge the support from the Knut and Alice Wallenberg Foundation through WBSQD2 project (Grant No. 2018.0071). This project is funded by the European Commission within Horizon Europe projects (Grant Nos. 101156088 and 101129663). The computations were enabled by resources provided by the National Academic Infrastructure for Supercomputing in Sweden (NAISS) and the Swedish National Infrastructure for Computing (SNIC) at NSC, partially funded by the Swedish Research Council through grant agreements no. 2022-06725 and no. 2018-05973. We acknowledge KIFÜ for awarding us access to computational resources based in Hungary.

Author contributions

R.B. designed the project and carried out the first-principles calculations with inputs from A.G. The manuscript was written by V.I., R.B., and G.B. with inputs from all co-authors. The work was supervised by V.I. and G.B.

Funding

Open access funding provided by Eötvös Loránd University.

Competing interests

The authors declare no competing interests.

Additional information

Supplementary information The online version contains supplementary material available at https://doi.org/10.1038/s41699-025-00559-z.

Correspondence and requests for materials should be addressed to Rohit Babar or Viktor Ivády.